Available online at www.sciencedirect.com

ScienceDirect

Geochimica et Cosmochimica Acta 231 (2018) 73–87

Geochimica et Cosmochimica Acta

www.elsevier.com/locate/gca

Multiple sulfur-isotopic evidence for a shallowly stratified ocean following the Triassic-Jurassic boundary mass extinction

Genming Luo [a,b,*], Sylvain Richoz [c,d], Bas van de Schootbrugge [e], Thomas J. Algeo [a,f,g], Shucheng Xie [a], Shuhei Ono [b], Roger E. Summons [b]

[a] State Key Laboratory of Biogeology and Environmental Geology and School of Earth Science, China University of Geosciences, Wuhan 430074, People's Republic of China

[b] Department of Earth, Atmospheric and Planetary Sciences, Massachusetts Institute of Technology, 77 Massachusetts Avenue, Cambridge, MA 02139, USA

[c] Institute for Earth Sciences, University of Graz, Nawi Graz, Heinrichstraße 26, 8020 Graz, Austria

[d] Department of Geology, Lund University, Sölvegatan 12, 22362 Lund, Sweden

[e] Institute of Earth Sciences, Marine Palynology and Paleoceanography, Utrecht University, Heidelberglaan 2, 3584 CD Utrecht, Netherlands

[f] State Key Laboratory of Geological Processes and Mineral Resources, China University of Geosciences, Wuhan 430074, People's Republic of China

[g] Department of Geology, University of Cincinnati, Cincinnati, Ohio 45221-0013, USA

Received 17 November 2016; accepted in revised form 11 April 2018; available online 18 April 2018

Abstract

The cause of the Triassic-Jurassic (Tr-J) boundary biotic crisis, one of the 'Big Five' mass extinctions of the Phanerozoic, remains controversial. In this study, we analyzed multiple sulfur-isotope compositions ($\delta^{33}S$, $\delta^{34}S$ and $\delta^{36}S$) of pyrite and S_{py}/TOC ratios in two Tr-J successions (Mariental, Mingolsheim) from the European Epicontinental Seaway (EES) in order to better document ocean-redox variations during the Tr-J transition. Our results show that upper Rhaetian strata are characterized by ^{34}S-enriched pyrite, low S_{py}/TOC ratios, and values of $\Delta^{33}S_{py}$ (i.e., the deviation from the mass-dependent array) lower than that estimated for contemporaneous seawater sulfate, suggesting an oxic-suboxic depositional environment punctuated by brief anoxic events. The overlying Hettangian strata exhibit relatively ^{34}S-depleted pyrite, high $\Delta^{33}S_{py}$, and S_{py}/TOC values, and the presence of green sulfur bacterial biomarkers indicate a shift toward to euxinic conditions. The local development of intense marine anoxia thus postdated the Tr-J mass extinction, which does not provide support for the hypothesis that euxinia was the main killing agent at the Tr-J transition. Sulfur and organic carbon isotopic records that reveal a water-depth gradient (i.e., more ^{34}S-, ^{13}C-depleted with depth) in combination with S_{py}/TOC data suggest that the earliest Jurassic EES was strongly stratified, with a chemocline located at shallow depths just below storm wave base. Shallow oceanic stratification may have been a factor for widespread deposition of black shales, a large positive shift in carbonate $\delta^{13}C$ values, and a delay in the recovery of marine ecosystems following the Tr-J boundary crisis.

Keywords: Oceanic anoxia; Oceanic stratification; Black shale; Sulfur isotopes; Isorenieratane; Epeiric sea

1. INTRODUCTION

The Triassic-Jurassic (Tr-J) transition at 201.3 million years ago (Ma) (Schoene et al., 2010) was characterized by upheavals resulting in the decimation of life both on

* Corresponding author at: State Key Laboratory of Biogeology and Environmental Geology and School of Earth Science, China University of Geosciences, Wuhan 430074, People's Republic of China.

E-mail address: gmluo@cug.edu.cn (G. Luo).

https://doi.org/10.1016/j.gca.2018.04.015

land and in the ocean (Olsen et al., 2002; McElwain et al., 2007; van de Schootbrugge et al., 2009). About 50% of genera and 80% of species of marine animals went extinct, including all conodonts and most scleractinian corals, ammonoids, and sphinctozoan sponges (Hautmann, 2012). The Hettangian stage (earliest Jurassic) was an important interval for marine biotic recovery, particularly among ammonoids (e.g., Guex et al., 2004). Widespread oceanic anoxia, possibly caused by increases in atmospheric pCO_2 and Earth-surface temperatures, is inferred to have been the main mechanism of the Tr-J marine extinction and an important factor limiting biotic recovery in Hettangian (van de Schootbrugge et al., 2008; Whiteside et al., 2010; Richoz et al., 2012; Jaraula et al., 2013). The evidence for oceanic anoxia is mainly from biomarkers of green sulfur bacteria (GSB; e.g., isorenieratane), whose metabolism requires both sunlight and H_2S and which are thus an indicator of photic-zone euxinia (Jaraula et al., 2013; Kasprak et al., 2015).

Earlier studies relying on GSB biomarker data may have underestimated the extent of oceanic anoxia during the Tr-J transition (e.g., Richoz et al., 2012) owing to a preservation bias against such biomarkers and the low sensitivity of the detection methods used (French et al., 2015). In the shallow European Epicontinental Seaway (EES), for example, GSB biomarkers have been identified in only a few layers, mainly in the basal Hettangian, with all other beds yielding quantities generally below instrumental detection limits (Richoz et al., 2012; Jaraula et al., 2013). In contrast, lithologic observations, such as the frequent occurrence of paper shale facies in sections across the EES (van de Schootbrugge et al., 2009), and trace-element data, which locally show concentrations well above lithogenic background values (Quan et al., 2008), provide evidence of a continuation of dysoxic to anoxic conditions well beyond the immediate Tr-J boundary interval. These uncertainties in the extent and duration of oceanic anoxia during the Tr-J transition make its relationship to the coeval mass extinction event and biotic recovery controversial. Therefore, other redox proxies are needed to complement GSB data in order to more fully document the redox history and spatial heterogeneities of the Tr-J boundary interval and unravel the temporal and causal relationships between mass extinction, biotic recovery, and oceanic anoxia.

The Tr-J boundary extinction interval was also accompanied by significant perturbations to the global carbon cycle, represented by large fluctuations in both carbonate and coeval organic carbon $\delta^{13}C$ values (e.g., Pálfy et al., 2001; Ward et al., 2001; Hesselbo et al., 2002; Williford et al., 2007; Ruhl et al., 2011; Bachan et al., 2012; Whiteside et al., 2010). These perturbations have been attributed to either voluminous eruptions of the Central Atlantic Magmatic Province (CAMP) or methane release from gas hydrates (e.g., Hesselbo et al., 2002; Ruhl et al., 2011). Either of these events may have had a significant impact on the biogeochemical cycling of sulfur, e.g., through emissions of SO_2 during CAMP eruptions (Tanner et al., 2004) or through intensified anaerobic oxidation of methane coupled with microbial sulfate reduction (Jørgensen et al., 2004). However, much less attention has been paid to the sulfur cycle than to the carbon cycle during this critical interval (Williford et al., 2009; Jaraula et al., 2013), despite their intimate coupling.

Recent instrumental advances have made possible the high-precision measurement of minor sulfur isotope concentrations (^{33}S and ^{36}S), allowing multiple sulfur isotopes to be applied to investigations of the sulfur biogeochemical cycle (e.g., Johnston, 2011). Empirical studies and culture experiments have shown that different sulfur metabolisms yield diagnostic isotopic fractionations of minor isotopes (e.g., Farquhar et al., 2003; Johnston et al., 2005a; Zerkle et al., 2010), and these differences have been identified in deep-time geological records (e.g., Johnston et al., 2005b). Coupled with $\delta^{34}S$ records, the introduction of minor isotopes provides greater insights into sulfur cycling processes and mechanisms of $\delta^{34}S$ variation (e.g., Leavitt et al., 2013; Sim et al., 2015; Masterson et al., 2016). Furthermore, multiple sulfur isotopes have been applied to reconstruction of paleo-sedimentary environmental conditions and paleo-seawater chemical compositions, e.g., seawater sulfate concentrations (e.g., Johnston et al., 2008; Shen et al., 2011; Scott et al., 2014; Luo et al., 2015; Zhang et al., 2015, 2017; Saitoh et al., 2017).

In this study, we analyzed multiple sulfur isotopes of pyrite and weight ratios of pyrite sulfur to total organic carbon (S_{py}/TOC) in two drillcores (Mariental and Mingolsheim) penetrating the Tr-J transition in Germany, representing continuous stratigraphic successions through the Tr-J transition that have been studied intensively (e.g., van de Schootbrugge et al., 2007, 2008, 2009; Quan et al., 2008; Richoz et al., 2012). The shallow-shelf settings of the study sites contained a rich fauna prior to the mass extinction event (van de Schootbrugge et al., 2009; Heunisch et al., 2010), permitting an examination of the relationship of marine sulfur cycle changes to the Tr-J boundary biotic crisis. On the basis of these data, we gained insights regarding sulfur cycling and redox conditions in the EES, as well as their relationships to carbon cycle perturbations and the contemporaneous faunal turnover.

2. GEOLOGICAL BACKGROUND

The two drillcores analyzed in this study, Mariental and Mingolsheim, are from northern and southern Germany, respectively (Fig. 1). Information about these two drillcores are presented in van de Schootbrugge et al. (2008, 2009, 2013), Quan et al. (2008), Heunisch et al. (2010), and Richoz et al. (2012). Paleogeographically, the study area was located within the epicontinental seas bordering the northwestern margin of the Tethys Ocean during the Tr-J transition (Dercourt et al., 2000) (Fig. 1). The Mingolsheim succession was deposited in the center of an intrashelf basin, the Langenbrückener Trough (Quan et al., 2008), whereas the Mariental succession was deposited in the Lower Saxony Basin, near the coast of the Bohemian Massif (van de Schootbrugge et al., 2009). The latter basin witnessed progressive rifting during the Late Triassic to Late Jurassic with contemporaneous syn-sedimentary faulting and salt diapirism, which resulted in a much thicker Lower Jurassic succession at Mariental relative to that at Mingol-

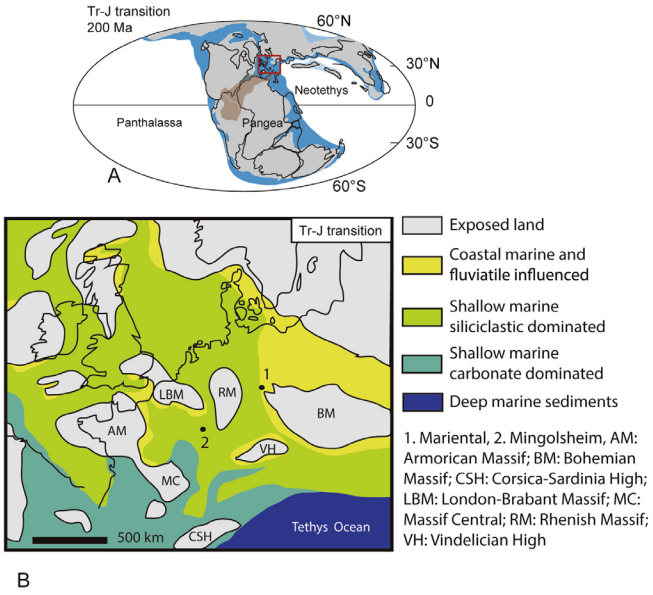

Fig. 1. Paleogeography and location of the two study cores (map redrawn from Ziegler, 1988; Dercourt et al., 2000). The red square in A represents area of map B. The brown field in A represents the approximate extent of the CAMP (McHone, 2003). (For interpretation of the references to colour in this figure legend, the reader is referred to the web version of this article.)

sheim (Heunisch et al., 2010). Although both study sections accumulated in shallow (i.e., <200 m) epicontinental seas, Mingolsheim represents a relatively deeper setting (ca. > 40 m) than Mariental (ca. < 40 m). Tr-J transition strata at Mingolsheim are uniformly laminated, whereas the correlative interval at Mariental contains hummocky cross-stratified beds reflecting sedimentation close to storm wave base. Furthermore, the sediments at Mingolsheim are finer-grained than those at Mariental, consistent with a deeper-water setting.

At Mingolsheim, the investigated stratigraphic interval ranges from the middle Rhaetian stage (Upper Triassic) to the lowermost Sinemurian stage (Lower Jurassic). The middle Rhaetian consists of fluviatile sandstones containing plant remains. The overlying units are the organic-rich *Rhaetavicula contorta* Beds (called *Contorta* Beds below for short), named after a characteristic late Triassic bivalve. The *Contorta* Beds are overlain by the uppermost Rhaetian Triletes Beds, a 7.6-m-thick, laminated, carbonate- and organic-poor claystone that lacks macrofossils, except for some minor shell hashes (van de Schootbrugge et al., 2009). The Psilonoten Limestone, a highly condensed, phosphatic and bioclastic limestone that overlies the Triletes Beds, contains psiloceratid ammonoids belonging to the lower Hettangian *Caloceras johnstoni* Subzone (van de Schootbrugge et al., 2009, and references therein). Overlying the Psilonoten Limestone, the Hettangian and basal Sinemurian consist of alternating limestones and shales with TOC generally higher than 3% (See Quan et al., 2008).

The investigated stratigraphic interval in the Mariental core also contains the *Contorta* and Triletes beds of the Rhaetian and Liassic α1 and Liassic α2 beds of the Hettangian. The Rhaetian units were deposited in a deltaic facies. The *Contorta* Beds consist of alternating flaser- and cross-bedded fine-grained sandstone and mudstone that can be correlated with the type section on a lithological basis (Heunisch et al., 2010). The overlying Triletes Beds are composed mainly of irregularly alternating laminae of mudstone and sandstone, with a 6-m-thick bed of fine-grained sandstone in the middle of the unit. The coarser siliciclastics exhibit sedimentary structures due to wave action and synsedimentary deformation (of possible seismic origin) (Lindstrom et al., 2015). Rhaetian sediments are conformable with overlying marine shales and intercalated sandstone beds of Hettangian age (Lias α1 and base of Lias α2) (Heunisch et al., 2010). The intervening sediments are composed of organic-rich claystones, containing partly fragmented plant remains and shell hashes.

The palynostratigraphy of the two study cores and their correlations were documented in van de Schootbrugge et al. (2009) and are briefly summarized below. The characteristic late Triassic pollen *Rhaetipollis germanicus* disappears at the base of the Triletes Beds in both cores, marking the base of the main extinction event (Figs. 2 and 3; see Section 5.5 for details). Upsection within the Triletes Beds, *Ricciisporites tuberculatus* (pollen), striated bisaccate pollen (generally thought to derive from peltasperm seed ferns such as *Lunatisporites rhaeticus*), and cycad pollen (e.g., *Ovalipollis ovalis*) decline in abundance, disappearing toward the formation top (Figs. 2 and 3). A similar gradual pattern of decline is observed for marine phytoplankton such as *Rhaetogonyaulax rhaetica*. Some Rhaetian dinocysts, e.g., *Suessia swabiana*, disappear at the base of the Triletes Beds. A key taxon for the Tr-J boundary itself, *Cerebropollenites thiergartii* (pollen) has been found directly above the Triletes Beds in the Mariental core, co-occurring with the spore *Kraeuselisporites reissingerii* (Fig. 2). In the

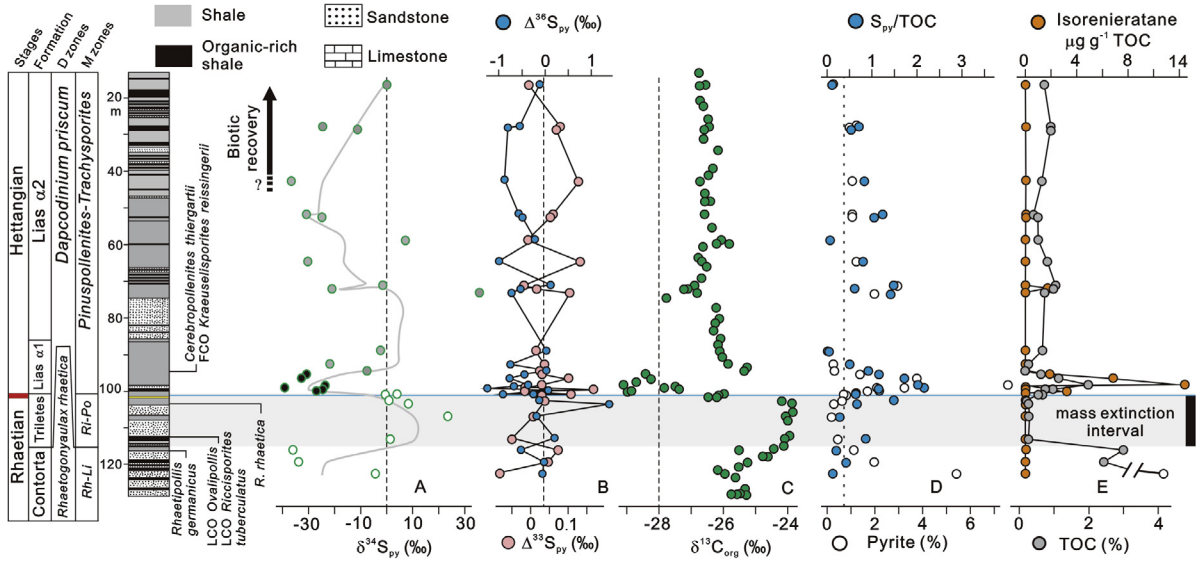

Fig. 2. Litho-, bio- and chemostratigraphy of the Mariental core in northern Germany. The gray line in A represents a three-point moving average, and the different shadings represent the three intervals that the samples are grouped in Fig. 5. The dashed line in B represents the estimated $\Delta^{33}S$ value of coeval seawater sulfate (+0.035‰; Wu et al., 2010). The dashed line in D is the general S_{py}/TOC value of oxic marine environments (0.36; Berner and Raiswell, 1983). The Triletes interval corresponds to the end-Triassic biotic crisis. Sulfur isotope and S_{py}/TOC data are original to this study; bio- and lithostratigraphic data are from van de Schootbrugge et al. (2009) and Richoz et al. (2012); TOC and isorenieratane data are from Richoz et al. (2012); $\delta^{13}C_{org}$ data are from van de Schootbrugge et al. (2013). FCO: first common occurrence; LCO: last common occurrence; D zone: Dinocyst zone; M zone: Minospore zone; *Rh-Li*: *Rhaetipollis-Limbosporites*; *Ri-Po*: *Ricciisporites-Polypodiisporites*.

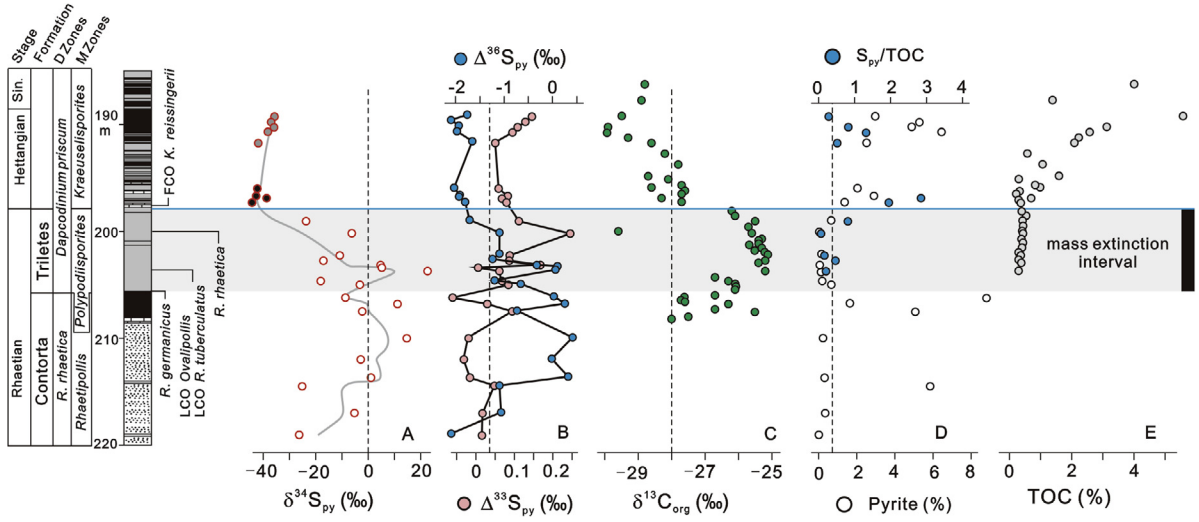

Fig. 3. Litho-, bio- and chemostratigraphy of the Mingolsheim core in southern Germany. The vertical lines in A, B and D are equivalent to those in Fig. 2. The different shadings in A represent the three intervals that the samples are grouped in Fig. 5.The Triletes interval corresponds to the end-Triassic biotic crisis. Sulfur isotope and S_{py}/TOC data are original to this study; bio- and lithostratigraphic data are from van de Schootbrugge et al. (2009); TOC and $\delta^{13}C_{org}$ data are from Quan et al. (2008). No GSB biomarker data are available for the Mingolsheim section.

global reference section and point (GSSP) for the Triassic-Jurassic boundary at Kuhjoch, Austria, the first common occurrence of *K. reissingerii* coincides with the first occurrence of the ammonoid *Psiloceras spelae*, the index fossil that defines the Tr-J boundary, lending support to the position of the Tr-J boundary based on *C. thiergartii*. Although *C. thiergartii* has not been found at Mingolsheim, the Tr-J boundary can be placed within the Psilonoten Limestone according to the first common occurrence of *K. reissingerii* (Fig. 3).

3. MATERIALS AND METHODS

3.1. Pyrite extraction

Bulk pyrite was analyzed in this study. Pyrite sulfur was extracted using the classic chromium reduction method. For each sample, from 0.5 to 8 g of rock powders were reacted with 6-M HCl in order to remove any carbonate and acid-volatile sulfur (AVS). The acid residue was cleaned with deionized water until neutralized and then dried in an oven at 60 °C for 24 h. A chromous chloride ($CrCl_2$) solution was prepared by reduction of chromic chloride ($CrCl_3$) using granulated elemental Zn under a N_2 atmosphere. The acid residue was placed in a reaction vessel that was connected to an Erlenmeyer flask trap containing 40 ml of zinc acetate, between which a trap containing deionized water was placed. The system was then flushed with N_2 for approx. 20–30 min, after which 40 ml of chromous chloride ($CrCl_2$), 10 ml of ethanol, and 20 ml of 6-M HCl were injected into the reaction vessel through a plastic syringe. The mixture was allowed to boil in the reaction vessel for 2 h with a N_2 flow through the system adjusted to maintain a constant flow of 2–3 bubbles per second into the Erlenmeyer flask. The evolved H_2S was collected in the Zn-acetate trap as Zn sulfide (ZnS). Lastly, ~1–3 ml of silver nitrate ($AgNO_3$) was added to the Erlenmeyer flask in order to precipitate silver sulfide (Ag_2S) that was then cleaned with DI water.

3.2. Sulfur isotope analysis

Multiple-sulfur isotope (^{32}S, ^{33}S, ^{34}S, and ^{36}S) compositions were measured according to the method of Ono et al. (2012), which is briefly described here. Approximately 2 mg of Ag_2S were reacted with elemental fluorine for >6 h at 300 °C. The evolved SF_6 was purified by a gas chromatograph equipped with a column packed with a 5-Å molecular sieve that was followed by a column packed with HayeSep Q. Isotope ratios of the purified SF_6 were measured using a magnetic-sector isotope ratio mass spectrometer (Thermo Finnigan MAT 253) operated in the dual-inlet mode. Replicate analyses ($n = 28$) of a reference material (IAEA-S-1; $\delta^{34}S = -0.3‰$; $\Delta^{33}S = 0.100‰$; $\Delta^{36}S = -0.57‰$) yielded 2σ (two standard deviations) of 0.26‰, 0.014‰, and 0.19‰ for $\delta^{34}S$, $\Delta^{33}S$ and $\Delta^{36}S$, respectively. Sulfur isotope ratios are reported using the conventional delta notation:

$$\delta^{x}S = 1000 \times \left({}^{x}R_{sample}/{}^{x}R_{VCDT} - 1\right) \quad (1)$$

where ${}^{x}R_{sample}$ and ${}^{x}R_{VCDT}$ are the isotope ratios ${}^{x}S/{}^{32}S$ (x = 33, 34 or 36) of the sample and VCDT (Vienna Canyon Diablo Troilite), respectively. The isotope ratios of VCDT (^{x}RVCDT) are defined by the international reference material (IAEA-S1) to be −0.055‰, −0.300‰, and −1.14‰ for $\delta^{33}S$, $\delta^{34}S$ and $\delta^{36}S$, respectively. The following definitions for $\Delta^{x}S$ are used (Ono et al., 2006):

$$\Delta^{33}S = 1000 \times [\ln(\delta^{33}S/1000 + 1) - 0.515 \times \ln(\delta^{34}S/1000 + 1)] \quad (2)$$

$$\Delta^{36}S = 1000 \times [(\ln(\delta^{36}S/1000 + 1) - 1.91 \times \ln(\delta^{34}S/1000 + 1)] \quad (3)$$

4. RESULTS

The lithologies of the study samples are mainly mudstone and fine siltstone. The pyrite content of all samples from both sections ranges from 0.1% to 9.0%, with two intervals containing abundant pyrite located directly below and above the Triletes Beds (Figs. 2 and 3). S_{py}/TOC values range from 0.05 to 2.86, showing large stratigraphic variability with the highest values generally located in basal beds of the Hettangian (Figs. 2 and 3).

Pyrite $\delta^{34}S$ values in both sections show considerable variation, ranging from ca. −43‰ to +10‰ (Figs. 2 and 3). Except for a few layers, most samples from the uppermost Triassic *Contorta* and Triletes Beds in both sections yield ^{34}S-enriched pyrite, with $\delta^{34}S$ values varying around 0‰. At Mingolsheim, a distinct negative shift in $\delta^{34}S$, from ~0‰ to <−40‰, starts in the uppermost Triletes Beds and reaches a minimum at the base of the overlying beds with little subsequent change upsection within the Hettangian. The negative shift in pyrite $\delta^{34}S$ values from the uppermost Triletes Beds to the overlying units is also present in the Mariental core. Compared with Mingolsheim, the pyrite $\delta^{34}S$ profile at Mariental is more complex, with a rebound of $\delta^{34}S$ values to higher values before a second negative shift to values around −30‰ within the Hettangian. High-resolution biostratigraphic correlation of Hettangian strata between the two study sections is not possible at present. This spatial difference may have been caused by different redox conditions in the two study areas as Mingolsheim was located in a deeper-water setting (see Section 2).

Pyrite $\Delta^{33}S$ and $\Delta^{36}S$ values range from −0.08‰ to +0.24‰ and from −2.10‰ to +1.40‰, respectively (Figs. 2, 3 and SI). Relative to the estimated $\Delta^{33}S$ value of coeval seawater sulfate (ca. +0.035‰; Wu et al., 2010), pyrite $\Delta^{33}S$ is more variable at Mariental than at Mingolsheim (Figs. 2 and 3). At both sites, pyrite $\Delta^{33}S$ values in the *Contorta* and Triletes interval are generally lower than the estimated coeval seawater sulfate $\Delta^{33}S$ value, whereas most Hettangian samples have $\Delta^{33}S$ values higher than seawater sulfate, although several layers with $\Delta^{33}S_{py}$ values lower than seawater sulfate are present in the Mariental core. The $\Delta^{36}S$ values generally display inverse variation to $\Delta^{33}S$ values, suggesting similar processes governing the variations in both parameters (Figs. 2 and 3). An negative correlation is present in the Mariental core with a slope ($\Delta^{36}S/\Delta^{33}S$) close to the theoretically calculated one (Fig. 4; Ono et al., 2006). The samples from the Triassic part of the Mingolsheim core conform to the regression trend of the Mariental samples, but those from the Hettangian interval have much lower $\Delta^{36}S$ values (−1‰ to −2‰) that deviate from the $\Delta^{36}S/\Delta^{33}S$ regression defined above (Fig. 4). These data potentially provide constraints on the sources of multiple sulfur isotope fractionations related to mass-dependent processes. As the specific mechanism responsible for these low $\Delta^{36}S$ values is uncertain, it will not be discussed further.

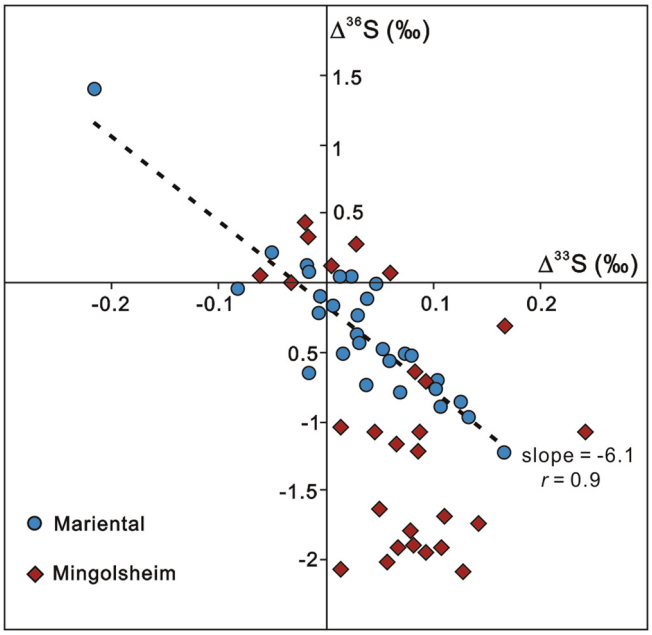

Fig. 4. Cross-plot of $\Delta^{33}S$ versus $\Delta^{36}S$ of pyrite in the Mariental (blue dots) and Mingolsheim (red diamonds) sections. (For interpretation of the references to colour in this figure legend, the reader is referred to the web version of this article.)

5. DISCUSSION

5.1. Environments of pyrite formation

Pyrite sulfur is generally sourced from microbial sulfate reduction (MSR), in which sulfate reduction is coupled with organic matter remineralization or H_2 oxidation, or from microbial sulfur disproportionation (MSD), in which intermediate oxidation-state sulfur compounds, such as elemental sulfur, are disproportionated to H_2S and sulfate. Both microbial processes induce substantial fractionations (ca. 10–70‰) in sulfur isotopes depending on the specific microbial metabolisms and the availability and types of electron donors (e.g., Habicht and Canfield, 1997; Sim et al., 2011; Leavitt et al., 2013). H_2S produced via MSR and MSD is generally depleted in ^{34}S, which is commonly recorded by sulfide phase in sediments (e.g., pyrite). In addition to microbial fractionation, the availability of sulfate is an important factor affecting the sulfur isotopic composition of pyrite (e.g., Fike et al., 2015). For example, in a restricted system (e.g., deep sediment porewater) in which the rate of sulfate supply is less than its rate of consumption, bulk pyrite $\delta^{34}S$ values can evolve to values close to, or higher than, contemporaneous seawater sulfate $\delta^{34}S$ values (e.g., Fike et al., 2015). In order to understand the processes underlying $\delta^{34}S_{py}$ variation, it is necessary to consider the environment of pyrite formation.

Multiple proxies have been proposed to differentiate environments of pyrite formation, i.e., open versus closed systems. Firstly, pyrite in sediments deposited in euxinic environments is generally formed in open systems such as the water column or porewaters of near-surface sediments. Many proxies are available for identification of euxinic environments in deep time, such as iron species (Lyons and Severmann, 2006), redox-sensitive trace element concentrations (Algeo and Maynard, 2004), and biomarkers for GSB or purple sulfur bacteria (PSB) that specifically indicate development of euxinia within the photic zone (e.g., French et al., 2015; Whiteside and Grice, 2016). Furthermore, anoxic/euxinic environments are also generally characterized by high concentrations of organic carbon and pyrite sulfur (e.g., Berner and Raiswell, 1983). Secondly, the morphology and size distribution of pyrite crystals can be used to identify pyrite formed in an open system (e.g., Wilkin et al., 1997). Pyrite framboids with diameters <5 μm are generally formed in a euxinic water column (e.g., Wilkin et al., 1997; Wignall et al., 2007). Thirdly, pyrite sulfur isotopes also can differentiate among environments of pyrite formation. In open systems, fractionation during MSR or MSD is well expressed, yielding strongly ^{34}S-depleted pyrite, in contrast to closed systems in which little to no fractionation occurs. Furthermore, pyrite $\delta^{34}S$ values in an open system generally show a limited range of variation, whereas the $\delta^{34}S$ values in a closed system tend to exhibit much greater variation (e.g., see Luo et al., 2015, and references therein).

In addition to the proxies above, pyrite $\Delta^{33}S$ ($\Delta^{33}S_{py}$) also can provide information about environments of pyrite formation. In an open system in which MSR is not limited by sulfate availability, $\Delta^{33}S_{py}$ can be estimated through the following equation on the basis of seawater sulfate $\Delta^{33}S$ ($\Delta^{33}S_{ss}$):

$$\Delta^{33}S_{py} = \Delta^{33}S_{ss} + 1000 \times \ln\left({}^{34}\alpha_{py-ss^{\lambda}} / {}^{34}\alpha_{py-ss^{0.515}}\right) \quad (4)$$

where ${}^{34}\alpha_{py\text{-}ss}$ represents the fractionation of ^{34}S during MSR, and λ ($\lambda = {}^{33}\alpha_{py\text{-}ss}/{}^{34}\alpha_{py\text{-}ss}$) represents the coefficient between fractionation of ^{33}S and ^{34}S during MSR. Experiments have shown that the λ values of MSR are generally <0.515 (Johnston et al., 2005a,b), resulting in $\Delta^{33}S_{py} > \Delta^{33}S_{ss}$ for $\alpha_{py\text{-}ss} < 1.0$(note that $\alpha_{py\text{-}ss}$ is generally 0.94–

0.97 in modern marine systems; Johnston et al., 2005a,b) (Fig. 5A). This pattern has been observed in modern stratified euxinic basins such as the Black Sea (e.g., Canfield et al., 2010; Li et al., 2010; Scheiderich et al., 2010). In closed systems, Rayleigh distillation causes the $\delta^{34}S$ and $\Delta^{33}S$ of instantaneously formed pyrite and residual sulfate to increase (black dashed arrows, Fig. 5A) (Ono et al., 2006). Consequently, the $\delta^{34}S_{py}$ and $\Delta^{33}S_{py}$ values of accumulated pyrite can be close to those of the original seawater sulfate (e.g., red arrow, Fig. 5A). Although $\Delta^{33}S_{py}$ is larger than $\Delta^{33}S_{ss}$ in both systems, $\delta^{34}S_{py}$ values can be used to differentiate open from closed systems owing to the extremely low $\delta^{34}S_{py}$ values of open systems (Fig. 5A).

A mixing process can yield a reservoir having a $\Delta^{33}S$ value lower than that of the sources (Ono et al., 2006). Therefore, if a pyrite sample consists of multiple endmembers (i.e., differently sourced pyrite fractions), the $\Delta^{33}S$ value of the bulk pyrite may be lower than that of any individual endmember. In settings characterized by frequent redox variations, pyrite commonly represents a mixture of two endmembers, i.e., one representing partial sulfate reduction in a sulfate-unlimited environment (e.g., anoxic water column or sediment-surface porewater) and the other representing quantitative sulfate reduction in a sulfate-limited environment (e.g., anoxic deep porewater below an oxic-suboxic water column). In this case, the $\Delta^{33}S_{py}$ values should be lower than the contemporaneous seawater sulfate $\Delta^{33}S_{ss}$ values (Fig. 5A; Sim et al., 2015), and the $\delta^{34}S_{py}$ values would be located between those of the two endmembers, with the absolute values depending on the mixing ratio. In summary, in order to better understand the environment of pyrite formation, an approach integrating the proxies discussed above is most useful.

5.2. Variations in redox conditions of the European Epicontinental Seaway

Mainly oxic water column depositional conditions are inferred for the Triletes Beds and the underlying *Contorta* Beds at both study sections on the basis of generally high $\delta^{34}S_{py}$ values (~0‰), representing closed-system sulfide production in deep sediment porewater (Fig. 5; Canfield and Farquhar, 2009). This redox inference is supported by the generally low S_{py}/TOC values and the absence of GSB biomarkers in these beds. It is interesting to note that, in some horizons, the $\Delta^{33}S_{py}$ values are lower than the expected coeval seawater $\Delta^{33}S_{ss}$ values (estimated at +0.035‰, Wu et al., 2010; Figs. 2, 3, 5), implying that the pyrite in these horizons consists of two endmembers, i.e., pyrite formed through partial sulfate reduction in a sulfate-unlimited environment and that formed through quantitative sulfate reduction in sulfate-limited environment (e.g., Shen et al., 2011; Zhang et al., 2015, 2017). Therefore, these $\Delta^{33}S_{ss}$ values suggest that, during deposition of the *Contorta* and Triletes beds, the prevailing oxic-suboxic conditions were interrupted by brief episodes of anoxia/euxinia in the water column or uppermost sediment column (Fig. 6), which is also supported by sporadic low $\delta^{34}S_{py}$ and high S_{py}/TOC values (Figs. 2 and 3). It should be noted that the operation of MSD may yield $\Delta^{33}S_{py}$ values lower than $\Delta^{33}S_{ss}$ values because the λ value of MSD estimated from limited experiments is close to 0.515 (i.e., higher than that of MSR) (e.g., Johnston et al., 2005a,b; Zhang et al., 2015). However, the generally high $\delta^{34}S_{py}$ values in the *Contorta* and Triletes beds suggest that MSD was of limited importance.

Multiple lines of evidence suggest that local shallow-marine redox conditions in the EES were significantly perturbed during the Tr-J transition, and that a euxinic water column developed during the early Hettangian (Richoz et al., 2012; Jaraula et al., 2013; Kasprak et al., 2015). The shift toward greater oxygen deficiency during the early Hettangian is documented by a significant increase in S_{py}/TOC ratios in the two study sections (to 2.86) relative to those typical of oxic-suboxic marine facies (~0.36) (Berner and Raiswell, 1983) (Fig. 5B). Meanwhile, euxinic conditions are supported by high concentrations of GSB biomarkers observed at the base of the Hettangian at Mari-

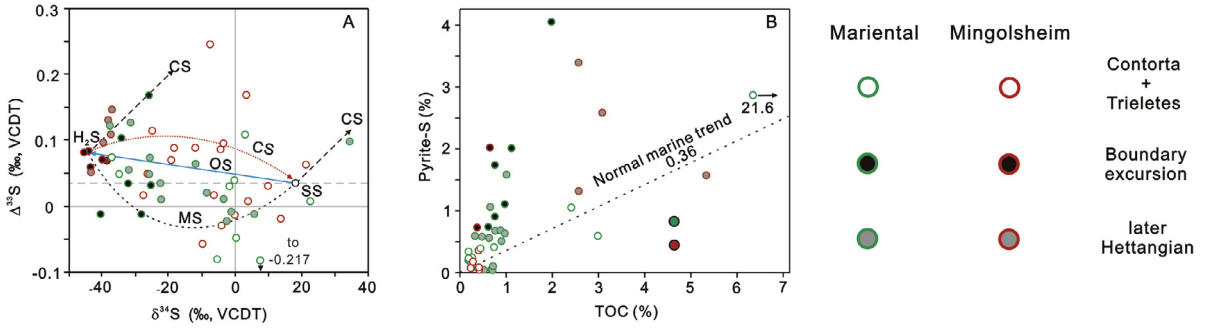

Fig. 5. (A) $\Delta^{33}S$ versus $\delta^{34}S$ of pyrite. (B) Pyrite content versus TOC. In A, the black circle represents the estimated multiple sulfur isotope composition of seawater sulfate (SS) during the Tr-J transition. The blue arrow shows the multiple sulfur isotopic evolution of pyrite (H_2S) produced by MSR in an open system; the slope of this line is defined by λ. The black dashed arrows represent the variation trends of the isotopic compositions of instantaneous H_2S and residual sulfate in a closed system, respectively, according to Ono et al. (2006). The red pointed arrow represents multiple sulfur isotopic compositions of pyrite formed in a closed system. The black dashed curve shows variation in multiple sulfur isotopic compositions of pyrite owing to mixing of two endmembers, i.e., early early-diagenetic pyrite in an open system and late early-diagenetic pyrite in a closed system with quantitative sulfate reduction. CS: closed system. OS: open system. MS: mixing system. In B, the dashed line represents the S_{py}/TOC ratio of normal marine sediments (Berner and Raiswell, 1983). (For interpretation of the references to colour in this figure legend, the reader is referred to the web version of this article.)

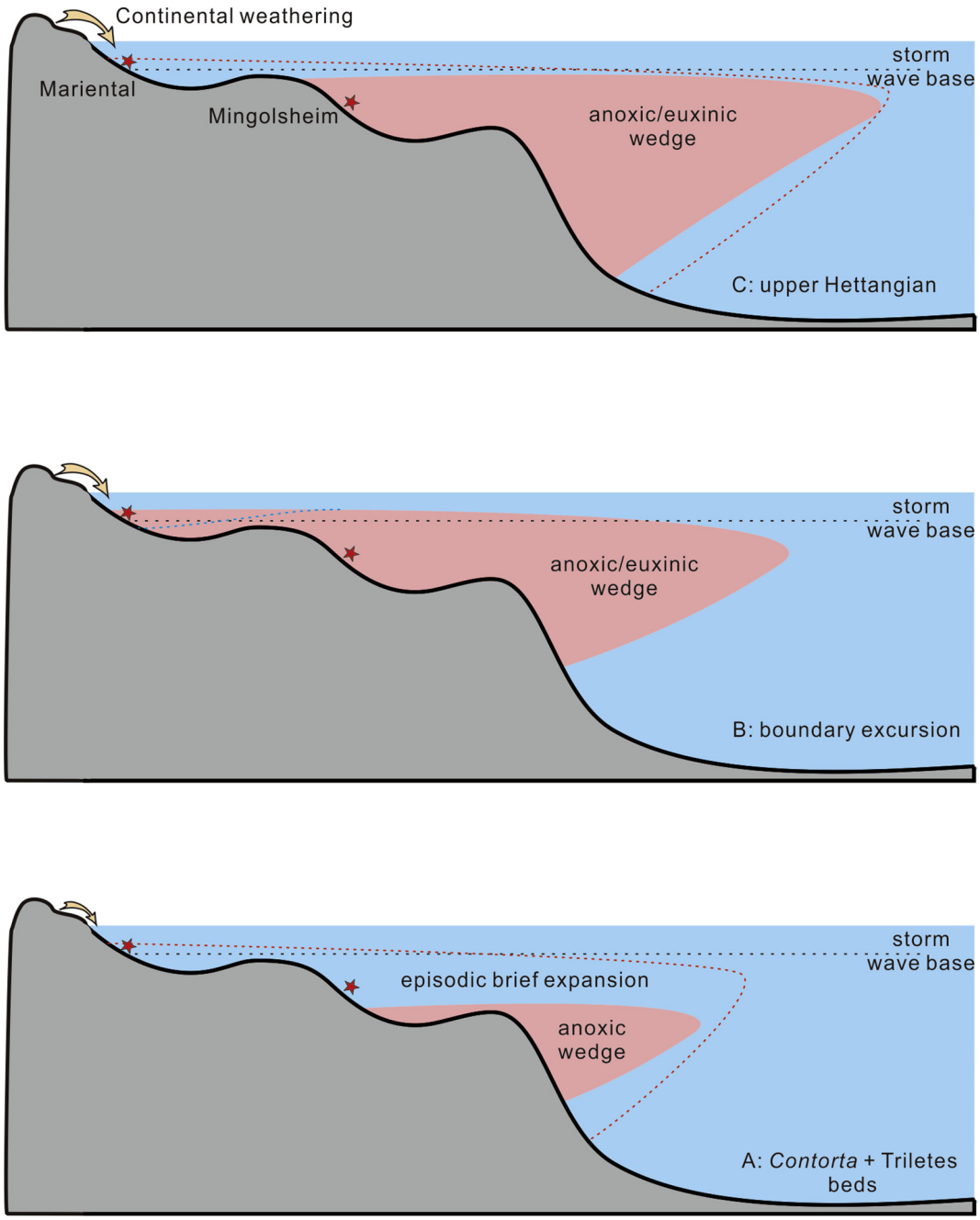

Fig. 6. Schematic figures showing the spatial and temporal variations in redox condition in the European Epicontinental Seaway during the Tr-J transition according to pyrite multiple sulfur isotope compositions and S_{py}/TOC data for Mariental and Mingolsheim. The dashed red line represents episodic brief expansion of the anoxic/euxinic wedge, whereas the blue dashed line suggests that the anoxic/euxinic wedge was punctuated by oxic/suboxic conditions in shallow-water environments such as at Mariental. Anoxic/euxinic wedge size is based on the carbonate uranium isotope data of Jost et al. (2017). The size of the arrows represents the flux of nutrients carried into the ocean. (For interpretation of the references to colour in this figure legend, the reader is referred to the web version of this article.)

ental (Fig. 2; Richoz et al., 2012) and by high framboidal pyrite content (Heunisch et al., 2010). Low $\delta^{34}S_{py}$ values suggest that the pyrite was generated in a sulfate-unlimited water column or sediment-surface porewater, supporting the occurrence of anoxia at that time. On the basis of the above discussion on the framework of $\delta^{34}S$-$\Delta^{33}S$, pyrite sulfur isotopes (Fig. 5A) suggest that the anoxic event at the base of the Hettangian may have been punctuated by brief oxic/suboxic events in the shallow-water Mariental section, but that anoxia may have been persistent (uninterrupted) in the deeper-water Mingolsheim section (Fig. 6). These observations lend support to our hypothesis that a large negative shift in pyrite $\delta^{34}S$ at the Tr-J boundary in both study sections was due to a transi-

tion from oxic to euxinic redox conditions in the EES water column (see Section 5.3).

Above the basal Hettangian, redox conditions became more spatially and temporally variable. $\delta^{34}S_{py}$ values remained consistently low at Mingolsheim, whereas the correlative interval at Mariental exhibits more variable and generally higher $\delta^{34}S_{py}$ values (Figs. 2 and 3). Uniformly low $\delta^{34}S_{py}$ values at Mingolsheim are consistent with a location below the chemocline, where MSR occurred in a sulfate-unlimited anoxic water column. This inference is supported by high $\Delta^{33}S_{py}$ values, generally high TOC and pyrite contents, and high S_{py}/TOC ratios (Figs. 3 and 5). On the other hand, the Mariental section was located close to the chemocline, leading to frequent secular redox variation, as shown by episodically low S_{py}/TOC values (Fig. 2) and the presence of GSB biomarkers (Richoz et al., 2012). When the chemocline was below the sediment–water interface, MSR occurred mainly in sulfate-limited sediment porewaters, yielding higher and more variable $\delta^{34}S_{py}$ values, but when the chemocline rose into the water column, MSR yielded lower and more uniform $\delta^{34}S_{py}$ values. Both endmember scenarios generated $\Delta^{33}S_{py} > \Delta^{33}S_{ss}$, but the mixing of pyrites formed under sulfate-limited and sulfate-unlimited conditions produced intermediate $\delta^{34}S$ values having $\Delta^{33}S_{py} < \Delta^{33}S_{ss}$ (Fig. 5A). The dominance of medium- to coarse-grained cubic pyrite indicates formation mainly in sediment porewaters (Heunisch et al., 2010). The differences in sulfur chemistry and inferred redox conditions between the two study sections during the Hettangian are consistent with lithofacies evidence suggesting that Mingolsheim was located in a deeper-water setting than Mariental, an inference supported by water-depth gradients in organic carbon isotopic compositions (see Section 5.4).

5.3. Perturbations to marine sulfur cycle during Tr-J transition

The two main sinks for seawater sulfate are removal to the sediment in oxic phases such as gypsum or carbonate-associated sulfate and in reduced phases such as Fe-sulfides (principally pyrite) (e.g., Bottrell and Newton, 2006). Mass balance calculations indicate that an increase in the fraction of pyrite burial, a phenomenon commonly associated with expansion of oceanic anoxia, would lead to a positive shift in both sulfate and pyrite $\delta^{34}S$ over time if other parameters are stable (Fike et al., 2015). No high-resolution $\delta^{34}S_{CAS}$ dataset has been published yet for the Tr-J transition, but a low-resolution evaporite $\delta^{34}S$ dataset (Strauss, 1997) suggests that seawater sulfate $\delta^{34}S$ values may have increased by ~6‰ during the Tr-J transition. Williford et al. (2009) found a positive shift in reduced sulfur $\delta^{34}S$ values from ca. −30‰ to +20‰ in lower Hettangian strata at Kennecott Point (Haida Gwaii, British Columbia), the magnitude of which is much larger than that of the coeval evaporite $\delta^{34}S$ record, suggesting that factors other than the evolution of seawater sulfate $\delta^{34}S$ contributed to the observed large positive shift in $\delta^{34}S_{py}$ values.

The Tr-J transition interval of the two study sections exhibits pronounced variability in $\delta^{34}S_{py}$ values, especially in the shallower Mariental section (Figs. 2 and 3), but neither section shows a distinct positive shift through this interval. The high and scattered $\delta^{34}S_{py}$ values in the lower part of the Triletes Beds and the underlying *Contorta* Beds are ascribed to sulfate limitation in a closed system. Thus, pyrite in this interval is unlikely to have a syngenetic origin, an inference supported by petrographic data (Heunisch et al., 2010). Similar considerations may pertain to the Kennecott Point section, in which a shift around the Tr-J boundary toward higher and more variable pyrite $\delta^{34}S$ values was probably also due to development of a less-open sediment porewater system (Williford et al., 2009).

The large negative shift in $\delta^{34}S_{py}$ values observed in the uppermost Triletes Beds of both study sections can be ascribed mostly to a redox change from oxic/suboxic to anoxic conditions, although ^{34}S-depleted SO_2 released from the CAMP may have contributed to this negative shift (Tanner et al., 2004). Specifically, a transition from authigenic pyrite generated in sulfate-limited anoxic sediment porewater under an oxic water column to syngenetic pyrite produced in sulfate-unlimited conditions in an anoxic water column would have led to (1) a negative shift in $\delta^{34}S_{py}$ values, and (2) reduced variability in $\delta^{34}S_{py}$ values, both of which are observed in the two study sections (Figs. 2 and 3). This inference is supported by the presence of large amounts of framboidal pyrite at this level in the Mariental section (Heunisch et al., 2010). The more variable and generally higher $\delta^{34}S$ values in the Hettangian at Mariental relative to Mingolsheim (Figs. 2 and 3) may have been due to similar processes but with more frequent redox fluctuations at Mariental (see Section 5.2).

The small positive $\delta^{34}S$ shift in the Hettangian beds at Mingolsheim (from ca. −42‰ to −37‰; Fig. 3) may represent a perturbation to the exogenic sulfur cycle. Generation of these pyrites in an open system is indicated by multiple lines of evidence, e.g., consistent $\delta^{34}S$ values, $\Delta^{33}S_{py} > \Delta^{33}S_{sw}$ and high S_{py}/TOC values, and the magnitude of this positive is almost the same as that observed in the marine evaporite $\delta^{34}S$ record compiled by Strauss (1997). This shift can be ascribed to an increase in pyrite burial flux associated with widespread anoxia in the EES during the Hettangian, enriching seawater sulfate in ^{34}S. High-resolution sulfate $\delta^{34}S$ records based on carbonate-associated sulfate will be needed to fully understand the evolution of the sulfur cycle during the Tr-J transition.

The $\delta^{34}S$ values of the syngenetic pyrite analyzed here reveal that sulfur isotopic fractionation during the Tr-J transition was ~60‰ based on pyrite $\delta^{34}S$ of −45‰ to −40‰ in the basal Hettangian of the Mingolsheim section and coeval seawater sulfate $\delta^{34}S$ of +16‰ to +18‰ (Kampschulte and Strauss, 2004). This value is within the range of single-step MSR fractionation observed in culture experiments and natural environments (e.g., Canfield et al., 2010; Wu et al., 2010; Sim et al., 2011) and consistent with high seawater sulfate levels during the Tr-J transition (Lowenstein et al., 2003; Algeo et al., 2015). The substantial increase in $\Delta^{33}S$ concurrent with relatively stable $\delta^{34}S$ values in the uppermost Hettangian at Mingolsheim may have been due to changes in the microbial community linked to sulfur cycling (Figs. 3 and 5), for which biomarker evidence should be sought in the future.

5.4. Relationships between marine C- and S-cycle perturbations

The transition from the Triletes Beds to overlying Hettangian strata is characterized by concurrent sharp negative excursions in $\delta^{13}C_{org}$ and $\delta^{34}S_{py}$ in the two study sections (Figs. 2 and 3). The strong coherence between the C- and S-isotope profiles may have been caused by a common source, e.g., massive emissions of isotopically light CO_2 and SO_2 during the CAMP eruptions (Tanner et al., 2004). However, as discussed above, the sharp negative shifts in $\delta^{34}S_{py}$ were mainly caused by changes in redox conditions. Below, we consider how variations in $\delta^{13}C_{org}$ values also may have been linked to changes in local redox conditions and microbial community composition.

A negative shift in organic carbon $\delta^{13}C$ records is a well-established feature of the Tr-J transition. Many $\delta^{13}C_{org}$ profiles show two negative shifts, i.e., an 'initial' and a 'main' event. Generally, the initial shift was transient and located at the main extinction level, whereas the main shift was prolonged and located above the Tr-J boundary (e.g., Ward et al., 2001; Hesselbo et al., 2002; Guex et al., 2004; Wignall et al., 2007; Ruhl et al., 2011;Yager et al., 2017). In this context, a brief negative shift just below the Triletes Beds and a subsequent persistent negative shift above the Triletes Beds at Mingolsheim have been interpreted as representing the initial and main events, respectively (Quan et al., 2008). Our correlation of the Mingolsheim and Mariental sections suggests that a negative shift above the Triletes Beds represents the main event at Mariental, and that the initial event may have been recorded by a single sample located just below the Triletes Beds.

In contrast to $\delta^{13}C_{org}$ records, carbonate $\delta^{13}C$ profiles for the Tr-J boundary generally show a positive shift during the Tr-J transition (Bachan et al., 2012; Yager et al., 2017), although negative shifts as large as ~7‰ (Csövár, Hungary; Pálfy et al., 2001, 2007) have been reported. Recently, the primary origin of these negative $\delta^{13}C_{carb}$ shifts has been questioned owing to their absence in some Tr-J boundary sections and to evidence of strong late diagenesis in some sections containing the signal (Bachan et al., 2012; van de Schootbrugge et al., 2008). These considerations imply that factors other than the isotopic composition of inorganic C sources affected $\delta^{13}C_{org}$ values.

On the basis of significant positive correlations between $\delta^{13}C_{org}$ and the absolute abundances of phytoplankton, organic matter type was inferred to have been the main control on $\delta^{13}C_{org}$ values in these sections (van de Schootbrugge et al., 2013). However, variable inputs of terrestrial versus marine organic matter were rejected as an explanation for the negative $\delta^{13}C_{org}$ shifts owing to the uniformity of the host lithofacies (Hesselbo et al., 2002). Below, we suggest that temporal and spatial variations in $\delta^{13}C_{org}$ during the Hettangian are consistent with our S-isotope-based oceanic stratification model.

The $\delta^{34}S_{py}$ and $\delta^{13}C_{org}$ profiles at Mariental, after rebounding quickly (over 5 to 10 m) to higher values above the Tr-J boundary, become somewhat variable further upsection (Fig. 2). The similar patterns for $\delta^{13}C_{org}$ and $\delta^{34}S_{py}$ suggest that local environmental conditions may have strongly influenced organic carbon isotopic compositions, possibly through two mechanisms. First, organic matter remineralization can generate a large vertical $\delta^{13}C$ gradient in dissolved inorganic carbon (DIC) (i.e., lower $\delta^{13}C_{DIC}$ with depth), as observed in modern and ancient stratified basins (e.g., Song et al., 2013; van Breugel et al., 2005). Secondly, chemoautotrophs living in anoxic environments commonly generate larger carbon isotope fractionations during carbon fixation than eukaryotic algae, enriching the synthesized organic matter in ^{12}C (Hayes et al., 1999). For example, the $\delta^{13}C$ value of particle organic carbon (POC) below the chemocline has been found to be much lower (by as much as 10‰) than that of the POC overlying the chemocline (van Breugel et al., 2005). The substantial spatial heterogeneities in $\delta^{13}C_{carb}$ and $\delta^{13}C_{org}$ observed during the Tr-J transition may also have been caused by spatial differences in redox conditions that controlled organic matter mineralization (Yager et al., 2017). During the Tr-J transition, the $\delta^{13}C_{org}$ of organic matter from below the oceanic chemocline may have been lower than that of organic matter from the surface layer of the same basin. Therefore, we suggest that the sharp negative shift in $\delta^{13}C_{org}$ in the uppermost Triletes Beds, which coincided with a redox transition from oxic/suboxic to anoxic conditions, may have been influenced by redox-dependent changes in microbial community composition and DIC-$\delta^{13}C$ values. Further investigation will be required to test whether this process contributed to the coeval negative shift in $\delta^{13}C_{org}$ values observed in other sections.

The Hettangian exhibits lower $\delta^{13}C_{org}$ values at Mingolsheim than at Mariental. This difference may be ascribed to a higher fraction of terrestrial organic matter at Mariental, which was closer to continental sources. However, the $\delta^{13}C_{org}$ values immediately above the Triletes Beds are similar in the two sections, which make this interpretation unlikely. Rather, the difference in $\delta^{13}C_{org}$ values is consistent with a redox control, i.e., the location of the Mariental section above the chemocline may have resulted in a higher fraction of organic matter produced by aerobic organisms relative to the Mingolsheim section, which was located mainly below the chemocline and, thus, likely to have received more organic matter from chemoautotrophs. A similar stratified-ocean scenario has been inferred for the Mesoproterozoic and the Permian–Triassic transition (Luo et al., 2014a, 2014b). Thus, the $\delta^{13}C_{org}$ records of the present study sections lend support to the shallowly stratified-ocean hypothesis for the Hettangian.

5.5. Oceanic euxinia, mass extinction, and biotic recovery

Given that metazoans are obligate aerobes, expanded oceanic anoxia, especially H_2S-enriched anoxia (euxinia), has been commonly regarded as an important mechanism of marine mass extinction in Earth history (e.g., Whiteside and Grice, 2016). Given a stratified euxinic ocean, shallowing of the chemocline and release of H_2S into the ocean-surface layer and atmosphere may have proven lethal to metazoans in shallow-marine and terrestrial habitats (Kump et al., 2005). GSB-derived biomarkers have been identified at multiple Tr-J boundary sites and have

been invoked as the main evidence for widespread contemporaneous photic-zone euxinia (PZE; Richoz et al., 2012; Jaraula et al., 2013; Kasprak et al., 2015). However, the details about the temporal relationship between the end-Triassic mass extinction and the development of PZE remain unclear.

The Tr-J boundary biocrisis was characterized by high rates of extinction among red-plastid-containing phytoplankton (e.g., dinoflagellates and coccolithophorids) (van de Schootbrugge et al., 2007; Richoz et al., 2012), calcareous nanoplankton, and shelly macroinvertebrates (Kiessling et al., 2007; Mander et al., 2008). These extinctions occurred just prior to the Tr-J boundary, typically coinciding with or slightly preceding the 'initial' negative shift in carbon isotopic composition of organic matter (Figs. 2 and 3). At both Mariental and Mingolsheim, the extinction horizon is within the Triletes Beds, which represent a peculiar unit of carbonate-poor claystones that are devoid of any macrofossil remains but extremely rich in trilete fern spores (van de Schootbrugge et al., 2009, Richoz et al., 2012). Among Rhaetian marine phytoplankton, some taxa (e.g., the dinocyst *Suessia swabiana*) disappeared at the base of the Triletes Beds, whereas others (e.g., *Rhaetogonyaulax rhaetica*) declined gradually and disappeared near the top of the Triletes Beds (van de Schootbrugge et al., 2009). A similar pattern is evident among pollen taxa, suggesting that the terrestrial biocrisis also may have played out in a patchwork fashion (van de Schootbrugge et al., 2009, and references therein). For example, the characteristic late Triassic pollen *Rhaetipollis germanicus* disappeared at the base of the Triletes Beds, whereas *Ricciisporites tuberculatus*, striated bisaccate forms (generally thought to derive from peltasperm seed ferns such as *Lunatisporites rhaeticus*), cycad pollen (e.g., *Ovalipollis ovalis*), and the dinoflagellate cyst *Suessia swabiana* declined in abundance gradually and disappeared toward the top of the Triletes Beds (Figs. 2 and 3).

These observations show that the onset of the Tr-J biocrisis in both shallow-marine and land habitats predated the development of widespread oceanic euxinia recorded in the two study sections. A similar temporal relationship may be present in other areas. For example, at the St. Audrie's section in the UK and the Kennecott Point section in Canada, the concentration of GSB biomarkers is generally

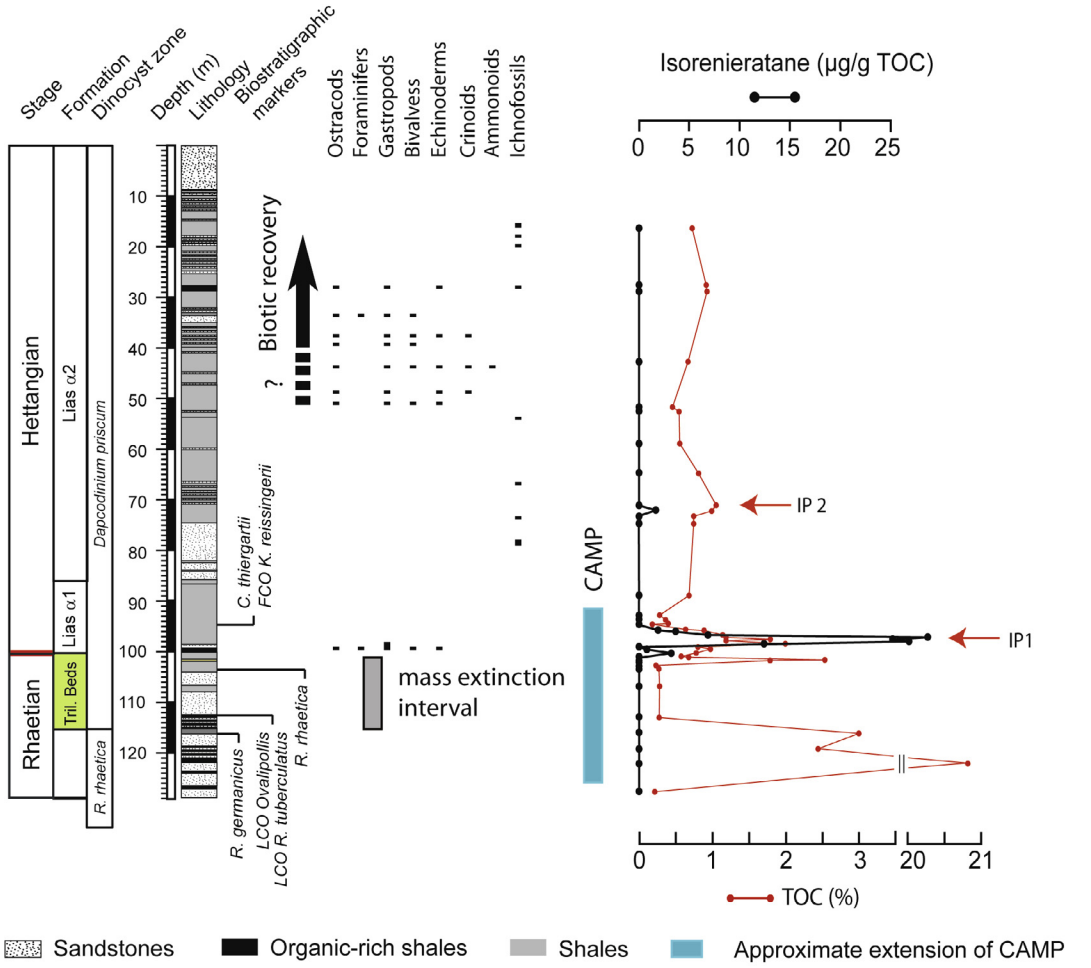

Fig. 7. Distribution of representative fossils and important events during the Tr-J transition at the Mariental section according to Heunisch et al. (2010) and Richoz et al. (2012). The other profiles are based on Fig. 2. IP: isorenieratane peak. CAMP: Central Atlantic Magmatic Province (Blackburn et al., 2013).

below detection limits in the end-Rhaetian beds corresponding to the Tr-J boundary biocrisis, whereas high concentrations have been reported from the overlying Hettangian strata (Jaraula et al., 2013; Kasprak et al., 2015). Consistent with the variations in local redox conditions reconstructed from sulfur isotopes and biomarker records, evidence for a global expansion of oceanic anoxia above the Tr-J boundary is provided by the uranium isotopic compositions of carbonates (Jost et al., 2017). All these records suggest that the development of widespread oceanic euxinia during the Tr-J transition postdated the end-Triassic marine and terrestrial biotic crises.

Expansion of oceanic anoxia following the Tr-J boundary mass extinction indicates that oceanic redox changes are unlikely to have been the main mechanism for the end-Triassic mass extinction, as hypothesized in some earlier studies (e.g., Kasprak et al., 2015). In this case, the immediate cause of mass mortality in both shallow-marine and terrestrial habitats must have been other global environmental changes, e.g., ocean acidification or elevated temperatures related to the release of large amounts of CO_2 or elevated concentrations of toxic materials, that were ultimately triggered by CAMP volcanism (McElwain et al., 1999; Thibodeau et al., 2016; Percival et al., 2017). Expansion of oceanic anoxia in the Hettangian is likely to have been the result of elevated temperatures, which reduced oxygen solubility in seawater, intensified vertical stratification, and possibly increased marine primary productivity through enhancement of continental weathering (e.g., Jaraula et al., 2013; Jost et al., 2017).

Widespread oceanic euxinia, although not being a primary cause of the Tr-J mass extinction, would have played an important role in modulating the tempo of the post-extinction marine biotic recovery. At Mariental, infaunal trace makers reappeared ~20 m above the Tr-J boundary and a moderately diverse marine invertebrate community containing ostracods and crinoids reappeared ~50 m above it (Fig. 7). The marine invertebrate recovery coincided with a positive shift in $\delta^{34}S_{py}$ values and a decrease in S_{py}/TOC values, suggesting a concurrent weakening of marine anoxia (Fig. 2). The early to middle Hettangian interval at Mariental witnessed the reappearance of many types of invertebrates. However, at Mingolsheim and other sections characterized by more severe oxygen deficiency, the marine biotic recovery was delayed until the late Hettangian (van de Schootbrugge et al., 2008, and references therein; Mander et al., 2008; Jaraula et al., 2013).

Widespread euxinic deep-water conditions may also account for deposition of black shales and a positive shift in $\delta^{13}C_{carb}$values in the Hettangian (van de Schootbrugge et al., 2008, 2009, 2013; Richoz et al., 2012). Although anoxia possibly delayed the recovery of animals, an increase in phosphorus abundance coupled with enhanced microbial nitrogen fixation (Quan et al., 2008) may have enhanced primary productivity during the post-extinction interval, which is supported by high concentrations of alkanes and isoprenoids in this interval (Jaraula et al., 2013). Anoxia promoted preservation of organic matter, leading to formation of black shale deposits. Widespread black shale deposition is consistent with an increase in the fraction of organic carbon burial, which was a likely cause of the concurrent positive shift in $\delta^{13}C_{carb}$ values, particularly since carbon entering the atmosphere–ocean system from the CAMP eruptions would have been isotopically light (e.g., Kump and Arthur, 1999).

6. CONCLUSIONS

Multiple sulfur isotopes of pyrite underwent large compositional variations during the Tr-J transition in the European Epicontinental Seaway (EES). The two study sites (Mariental and Mingolsheim) had mainly oxic-suboxic bottom waters during the Late Triassic Rhaetian Stage, although possibly punctuated by brief episodes of anoxia/euxinia. Pyrite $\delta^{34}S$ shows a large negative shift at the base of the Hettangian in both sections, synchronous with a negative $\delta^{13}C_{org}$ shift, high S_{py}/TOC ratios, and the appearance of GSB biomarkers. These changes document the development of widespread euxinia in the shallow EES postdating the end-Triassic mass extinction. This temporal relationship suggests that expanded oceanic anoxia was not the main cause of mortality among shallow-marine benthos during the end-Triassic mass extinction. Our multiple sulfur isotope data and S_{py}/TOC ratios suggest that the Hettangian ocean was stratified across the EES area with the chemocline located just below storm wave base. Euxinic conditions may have persisted for much of the ~2-Myr-long Early Jurassic Hettangian Stage (Schaltegger et al., 2008), affecting biotic recovery from the end-Triassic extinction, and contributing to widespread deposition of black shale and a positive shift in carbonate $\delta^{13}C$ values.

ACKNOWLEDGMENTS

We thank Bill Olszewski for assistance with sulfur isotope analysis, and Carmen Heunisch for sharing her pyrite morphology work. We send our sincere thanks to associate editor Tim Lyons and to the reviewers (William Leavitt, Ken Williford, Charles Diamond, and one anonymous) whose comments greatly improved the quality of this work. This study was supported by the National Key R&D Project of China (Gant No. 2016YFA0601104), 973 program (2013CB955704), the Chinese National Natural Science Foundation (Grant Nos. 41472170, 41730320) and the 111 project (Grant No. B08030).

APPENDIX A. SUPPLEMENTARY MATERIAL

Supplementary data associated with this article can be found, in the online version, at https://doi.org/10.1016/j.gca.2018.04.015.

REFERENCES

Algeo T. J. and Maynard J. B. (2004) Trace-element behavior and redox facies in core shales of Upper Pennsylvanian Kansas-type cyclothems. *Chem. Geol.* **206**, 289–318.

Algeo T. J., Luo G. M., Song H. Y., Lyons T. W. and Canfield D. E. (2015) Reconstruction of secular variation in seawater sulfate concentrations. *Biogeosciences* **12**, 2131–2151.

Bachan A., van de Schootbrugge B., Fiebig J., McRoberts C. A., Ciarapica G. and Payne J. L. (2012) Carbon cycle dynamics following the end-Triassic mass extinction: Constraints from paired δ13Ccarb and δ13Corg records. *Geochem. Geophys. Geosyst.* **13**(9). https://doi.org/10.1029/2012GC004150.

Berner R. A. and Raiswell R. (1983) Burial of organic carbon and pyrite sulfur in sediments over Phanerozoic time: a new theory. *Geochim. Cosmochim. Acta* **47**, 855–862.

Blackburn T. J., Olsen P. E., Bowring S. A., McLean N. M., Kent D. V., Puffer J., McHone G., Rasbury E. T. and Et-Touhami M. (2013) Zircon U-Pb geochronology links the end-triassic extinction with the central atlantic Magmatic Province. *Science* **340**, 941–945.

Bottrell S. H. and Newton R. J. (2006) Reconstruction of changes in global sulfur cycling from marine sulfate isotopes. *Earth Sci. Rev.* **75**, 59–83.

Canfield D. E. and Farquhar J. (2009) Animal evolution, bioturbation, an the sulfate concentration of the oceans. *Proc. Natl. Acad. Sci. USA* **106**, 8123–8127.

Canfield D. E., Farquhar J. and Zerkle A. L. (2010) High isotope fractionations during sulfate reduction in a low-sulfate euxinic ocean analog. *Geology* **38**, 415–418.

Dercourt J., Gaetani M., Vrielynck B., Barrier E., Biju-Duval B., Brunet M. F., Cadet J. P., Crasquin S. and Sandulescu M. (2000). Atlas Peri-Tethys, Palaeogeographical Maps, Paris, CCGM/CGMW, 269 pp.

Farquhar J., Johnston D. T., Wing B. A., Habicht K. S., Canfield D. E., Airieau S. and Thiemens M. H. (2003) Multiple sulphur isotopic interpretations of biosynthetic pathways: implications for biological signatures in the sulphur isotope record. *Geobiology* **1**, 27–36.

Fike D. A., Bradley A. S. and Rose C. V. (2015) Rethinking the ancient sulfur cycle. *Annu. Rev. Earth Planet. Sci.* **43**, 593–622.

French K. L., Rocher D., Zumberge J. E. and Summons R. E. (2015) Assessing the distribution of sedimentary C_{40} carotenoids through time. *Geobiology* **13**, 139–151.

Guex J., Bartolini A., Atudorei V. and Taylor D. (2004) High-resolution ammonite and carbon isotope stratigraphy across the Triassic-Jurassic boundary at New York Canyon (Nevada). *Earth Planet. Sci. Lett.* **225**, 29–41.

Habicht K. S. and Canfield D. E. (1997) Sulfur isotope fractionation during bacterial sulfate reduction in organic-rich sediments. *Geochim. Cosmochim. Acta* **61**, 5351–5361.

Hautmann M. (2012). Extinction: End-Triassic mass extinction. eLS (Wiley Online Library), http://doi.org/10.1002/9780470015902.a0001655.pub3.

Hayes J. M., Strauss H. and Kaufman A. J. (1999) The abundance of ^{13}C in marine organic matter and isotopic fractionation in the global biogeochemical cycle of carbon during the past 800 Ma *Chem. Geol.* **161**, 103–125.

Hesselbo S. P., Robinson S. A., Surlyk F. and Piasecki S. (2002) Terrestrial and marine extinction at the Triassic-Jurassic boundary synchronized with major carbon-cycle perturbation: A link to initiation of massive volcanism? *Geology* **30**, 251–254.

Heunisch C., Luppold F. W., Reinhardt L. and Röhling H. G. (2010) Palynofacies, bio- and lithostratigraphy at the Triassic/Jurassic boundary in the Mariental 1 borehole (Lappwald Syncline, Eastern Lower Saxony). *Z. Dtsch. Geol. Ges.* **161**, 51–98.

Jaraula C. M. B., Grice K., Twitchett R. J., Böttcher M. E., LeMetayer P., Dastidar A. G. and Opazo L. F. (2013) Elevated pCO_2 leading to Late Triassic extinction, persistent photic zone euxinia, and rising sea levels. *Geology* **41**, 955–958.

Johnston D. T. (2011) Multiple sulfur isotopes and the evolution of Earth's surface sulfur cycle. *Earth Sci. Rev.* **106**, 161–183.

Johnston D. T., Farquhar J., Wing B. A., Kaufman A. J., Canfield D. E. and Habicht K. S. (2005a) Multiple sulfur isotope fractionations in biological systems: A case study with sulfate reducers and sulfur disproportionators. *Am. J. Sci.* **305**, 645–660.

Johnston D. T., Wing B. A., Farquhar J., Kaufman A. J., Strauss H., Lyons T. W., Kah L. C. and Canfield D. E. (2005b) Active microbial sulfur disproportionation in the Mesoproterozoic. *Science* **310**, 1477–1479.

Johnston D. T., Farquhar J., Summons R. E., Shen Y. A., Kaufman A. J., Masterson A. and Canfield D. E. (2008) Sulfur isotope biogeochemistry of the Proterozoic McArthur Basin. *Geochim. Cosmochim. Acta* **72**, 4278–4290.

Jørgensen B. B., Böttcher M. E., Lüschen H., Neretin L. N. and Volkov I. I. (2004) Anaerobic methane oxidation and a deep H_2S sink generate isotopically heavy sulfides in Black Sea sediments. *Geochim. Cosmochim. Acta* **68**, 2095–2118.

Jost A. B., Bachan A., van de Schootbrugge B., Lau K. V., Weaver K. L., Maher K. and Payne J. L. (2017) Uranium isotope evidence for an expansion of marine anoxia during the end-Triassic extinction. *Geochem. Geophys. Geosyst.* **18**, 3093–3108.

Kampschulte A. and Strauss H. (2004) The sulfur isotopic evolution of Phanerozoic seawater based on the analysis of structurally substituted sulfate in carbonates. *Chem. Geol.* **204**, 255–286.

Kasprak A. H., Sepúlveda J., Price-Waldman R., Williford K. H., Schoepfer S. D., Haggart J. W., Ward P. D., Summons R. E. and Whiteside J. H. (2015) Episodic photic zone euxinia in the northeastern Panthalassic Ocean during the end-Triassic extinction. *Geology* **43**, 307–310.

Kiessling W., Aberhan M., Brenneis B. and Wagner P. J. (2007) Extinction trajectories of benthic organisms across the Triassic-Jurassic boundary. *Palaeogeogr. Palaeoclimatol. Palaeoecol.* **244**, 201–222.

Kump L. R. and Arthur A. (1999) Interpreting carbon–isotope excursions: carbonates and organic matter. *Chem. Geol.* **161**, 181–198.

Kump L. R., Pavlov A. and Arthur M. A. (2005) Massive release of hydrogen sulfide to the surface ocean and atmosphere during interval of oceanic anoxia. *Geology* **33**, 397–400.

Leavitt W. D., Halevy I., Bradley A. S. and Johnston D. T. (2013) Influence of sulfate reduction rates on the Phanerozoic sulfur isotope record. *Proc. Natl. Acad. Sci.* **110**, 11244–11249.

Li X., Gilhooly Iii W. P., Zerkle A. L., Lyons T. W., Farquhar J., Werne J. P., Varela R. and Scranton M. I. (2010) Stable sulfur isotopes in the water column of the Cariaco Basin. *Geochim. Cosmochim. Acta* **74**, 6764–6778.

Lindström S., Pedersen G. K., van de Schootbrugge B., Hansen K. H., Kuhlmann N., Thein J., Johansson L., Petersen H. I., Alwmark C., Dybkjær K., Weibel R., Erlström M., Nielsen L. H., Oschmann W. and Tegner C. (2015) Intense and widespread seismicity during the end-Triassic mass extinction due to emplacement of a large igneous province. *Geology* **43**, 387–390.

Lowenstein T. K., Hardie L. A., Timofeeff M. N. and Demicco R. V. (2003) Secular variation in seawater chemistry and the origin of calcium chloride basinal brines. *Geology* **31**, 857–860.

Luo G., Algeo T. J., Huang J., Zhou W., Wang Y., Yang H., Richoz S. and Xie S. (2014a) Vertical $\delta^{13}C_{org}$ gradients record changes in planktonic microbial community composition during the end-Permian mass extinction. *Palaeogeogr. Palaeoclimatol. Palaeoecol.* **396**, 119–131.

Luo G., Junium C. K., Kump L. R., Huang J., Li C., Feng Q., Shi X., Bai X. and Xie S. (2014b) Shallow stratification prevailed for ~1700 to ~1300 Ma ocean: Evidence from organic carbon isotopes in the North China Craton. *Earth Planet. Sci. Lett.* **400**, 219–232.

Luo G., Ono S., Huang J., Algeo T. J., Li C., Zhou L., Robinson A., Lyons T. W. and Xie S. (2015) Decline in oceanic sulfate levels during the early Mesoproterozoic. *Precambr. Res.* **258**, 36–47.

Lyons T. W. and Severmann S. (2006) A critical look at iron paleoredox proxies: New insights from modern euxinic marine basins. *Geochim. Cosmochim. Acta* **70**, 5698–5722.

Mander L., Twitchett R. J. and Benton M. J. (2008) Palaeoecology of the Late Triassic extinction event in the SW UK. *J. Geol. Soc. London* **165**, 319–332.

Masterson A. L., Wing B. A., Paytan A., Farquhar J. and JohnstonD T. (2016) The minor sulfur isotope composition of Cretaceous and Cenozoic seawater sulfate. *Paleoceanography* **31**, 2016PA002945.

McElwain J. C., Beerling D. J. and Woodward F. I. (1999) Fossil plants and global warming at the Triassic-Jurassic boundary. *Science* **285**, 1386–1390.

McElwain J. C., Popa M. E., Hesselbo S. P., Haworth M. and Surlyk F. (2007) Macroecological responses of terrestrial vegetation to climatic and atmospheric change across the Triassic/Jurassic boundary in East Greenland. *Paleobiology* **33**, 547–573.

McHone J. G. (2003) The Central Atlantic Magmatic Province: Insights from fragments of Pangea. Geophysical Monograph 136. *Am. Geophys. Union* **1-13**. https://doi.org/10.1029/136GM013.

Olsen P. E., Kent D. V., Sues H. D., Koeberl C., Huber H., Montanari A., Rainforth E. C., Fowell S. J., Sazajna M. J. and Hartline B. W. (2002) Ascent of dinosaurs linked to an iridium anomaly at the Triassic-Jurassic boundary. *Science* **296**, 1305–1308.

Ono S., Wing B., Johnston D., Farquhar J. and Rumble D. (2006) Mass-dependent fractionation of quadruple stable sulfur isotope system as a new tracer of sulfur biogeochemical cycles. *Geochim. Cosmochim. Acta* **70**, 2238–2252.

Ono S., Keller N. S., Rouxel O. and Alt J. C. (2012) Sulfur-33 constraints on the origin of secondary pyrite in altered oceanic basement. *Geochim. Cosmochim. Acta* **87**, 323–340.

Pálfy J., Demény A., Haas J., Hetényi M., Orchard M. J. and Veto I. (2001) Carbon isotope anomaly and other geochemical changes at the Triassic-Jurassic boundary from a marine section in Hungary. *Geology* **29**, 1047–1050.

Pálfy J., Demény A., Haas J., Carter E. S., Görög Á., Halász D., Oravecz-Scheffer A., Hetényi M., Márton E., Orchard M. J., Ozsvárt P., Vető I. and Zajzon N. (2007) Triassic-Jurassic boundary events inferred from integrated stratigraphy of the Csővár section, Hungary. *Palaeogeogr. Palaeoclimatol. Palaeoecol.* **244**, 11–33.

Percival L. M. E., Ruhl M., Hesselbo S. P., Jenkyns H. C., Mather T. A. and Whiteside J. H. (2017) Mercury evidence for pulsed volcanism during the end-Triassic mass extinction. *Proc. Natl. Acad. Sci.* **114**, 7929–7934.

Quan T. M., van de Schootbrugge B., Field M. P., Rosenthal Y. and Falkowski P. G. (2008) Nitrogen isotope and trace metal analyses from the Mingolsheim core (Germany): Evidence for redox variations across the Triassic-Jurassic boundary. *Global Biogeochem. Cycles* **22**, 002008.

Richoz S., van de Schootbrugge B., Pross J., Puttmann W., Quan T. M., Lindstrom S., Heunisch C., Fiebig J., Maquil R., Schouten S., Hauzenberger C. A. and Wignall P. B. (2012) Hydrogen sulphide poisoning of shallow seas following the end-Triassic extinction. *Nat. Geosci.* **5**, 662–667.

Ruhl M., Bonis N. R., Reichart G.-J., Sinninghe Damsté J. S. and Kürschner W. M. (2011) Atmospheric carbon injection linked to end-Triassic mass extinction. *Science* **333**, 430–434.

Saitoh M., Ueno Y., Matsu'ura F., Kawamura T., Isozaki Y., Yao J., Ji Z. and Yoshida N. (2017) Multiple sulfur isotope records at the end-Guadalupian (Permian) at Chaotian, China: Implications for a role of bioturbation in the Phanerozoic sulfur cycle. *J. Asian Earth Sci.* **135**, 70–79.

Schaltegger U., Guex J., Bartolini A., Schoene B. and Ovtcharova M. (2008) Precise U-Pb age constraints for end-Triassic mass extinction, its correlation to volcanism and Hettangian post-extinction recovery. *Earth Planet. Sci. Lett.* **267**, 266–275.

Scheiderich K., Zerkle A. L., Helz G. R., Farquhar J. and Walker R. J. (2010) Molybdenum isotope, multiple sulfur isotope, and redox-sensitive element behavior in early Pleistocene Mediterranean sapropels. *Chem. Geol.* **279**, 134–144.

Schoene B., Guex J., Bartolini A., Schaltegger U. and Blackburn T. J. (2010) Correlating the end-Triassic mass extinction and flood basalt volcanism at the 100 ka level. *Geology* **38**, 387–390.

Scott C., Wing B. A., Bekker A., Planavsky N. J., Medvedev P., Bates S. M., Yun M. and Lyons T. W. (2014) Pyrite multiple-sulfur isotope evidence for rapid expansion and contraction of the early Paleoproterozoic seawater sulfate reservoir. *Earth Planet. Sci. Lett.* **389**, 95–104.

Shen Y. A., Farquhar J., Zhang H., Masterson A., Zhang T. G. and Wing B. A. (2011) Multiple S-isotopic evidence for episodic shoaling of anoxic water during Late Permian mass extinction. *Nat. Commun.* **2**.

Sim M. S., Ono S. H., Donovan K., Templer S. P. and Bosak T. (2011) Effect of electron donors on the fractionation of sulfur isotopes by a marine Desulfovibrio sp. *Geochim. Cosmochim. Acta* **75**, 4244–4259.

Sim M. S., Ono S. and Hurtgen M. T. (2015) Sulfur isotope evidence for low and fluctuating sulfate levels in the Late Devonian ocean and the potential link with the mass extinction event. *Earth Planet. Sci. Lett.* **419**, 52–62.

Song H. Y., Tong J., Algeo T. J., Horacek M., Qiu H., Song H. J., Tian L. and Chen Z.-Q. (2013) Large vertical $\delta^{13}C_{DIC}$ gradients in Early Triassic seas of the South China craton: Implications for oceanographic changes related to Siberian Traps volcanism. *Global Planet. Change* **105**, 7–20.

Strauss H. (1997) The isotopic composition of sedimentary sulfur through time. *Palaeogeogr. Palaeoclimatol. Palaeoecol.* **132**, 97–118.

Tanner L. H., Lucas S. G. and Chapman M. G. (2004) Assessing the record and causes of Late Triassic extinctions. *Earth Sci. Rev.* **65**, 103–139.

Thibodeau A. M., Ritterbush K. A., Yager J. A., West A. J., Ibarra Y., Bottjer D. J., Berelson W. M., Bergquist B. A. and Corsetti F. A. (2016) Mercury anomalies and the timing of biotic recovery following the end-Triassic mass extinction. *Nat. Commun.* **7**, 11147.

van Breugel Y., Schouten S., Paetzel M., Nordeide R. and Sinninghe Damsté J. S. (2005) The impact of recycling of organic carbon on the stable carbon isotopic composition of dissolved inorganic carbon in a stratified marine system (Kyllaren Fjord, Norway). *Org. Geochem.* **36**, 1163–1173.

van de Schootbrugge B., Tremolada F., Rosenthal Y., Bailey T. R., Feist-Burkhardt S., Brinkhuis H., Pross J., Kent D. V. and Falkowski P. G. (2007) End-Triassic calcification crisis and blooms of organic-walled 'disaster species'. *Palaeogeogr. Palaeoclimatol. Palaeoecol.* **244**, 126–141.

van de Schootbrugge B., Payne J. L., Tomasovych A., Pross J., Fiebig J., Benbrahim M., Föllmi K. B. and Quan T. M. (2008) Carbon cycle perturbation and stabilization in the wake of the Triassic-Jurassic boundary mass-extinction event. *Geochem. Geophys. Geosyst.* **9**. https://doi.org/10.1029/2007GC001914.

van de Schootbrugge B., Quan T. M., Lindstrom S., Puttmann W., Heunisch C., Pross J., Fiebig J., Petschick R., Rohling H. G., Richoz S., Rosenthal Y. and Falkowski P. G. (2009) Floral changes across the Triassic/Jurassic boundary linked to flood basalt volcanism. *Nat. Geosci.* **2**, 589–594.

van de Schootbrugge B., Bachan A., Suan G., Richoz S. and Payne J. L. (2013) Microbes, mud and methane: cause and consequence of recurrent Early Jurassic anoxia following the end-Triassic mass extinction. *Palaeontology* **56**, 685–709.

Ward P. D., Haggart J. W., Carter E. S., Wilbur D., Tipper H. W. and Eans T. (2001) Sudden productivity collapse associated with the Triassic-Jurassic boundary mass extinction. *Science* **292**, 1148–1151.

Whiteside J. H. and Grice K. (2016) Biomarker records associated with mass extinction events. *Annu. Rev. Earth Planet. Sci.* **44**, 581–612.

Whiteside J. H., Olsen P. E., Eglinton T., Brookfield M. E. and Sambrotto N. R. (2010) Compound-specific carbon isotopes from Earth's largest flood basalt eruptions directly linked to the end-Triassic mass extinction. *Proc. Natl. Acad. Sci.* **107**, 6721–6725.

Wignall P. B., Zonneveld J. P., Newton R. J., Amor K., Sephton M. A. and Hartley S. (2007) The end Triassic mass extinction record of Williston Lake, British Columbia. *Palaeogeogr. Palaeoclimatol. Palaeoecol.* **253**, 385–406.

Wilkin R. T., Arthur M. A. and Dean W. E. (1997) History of water-column anoxia in the Black Sea indicated by pyrite framboid size distributions. *Earth Planet. Sci. Lett.* **148**, 517–525.

Williford K. H., Ward P. D., Garrison G. H. and Buick R. (2007) An extended organic carbon-isotope record across the Triassic-Jurassic boundary in the Queen Charlotte Islands, British Columbia, Canada. *Palaeogeography, Palaeoclimatology and Palaeoecology* **244**, 290–296.

Williford K. H., Foriel J., Ward P. D. and Steig E. J. (2009) Major perturbation in sulfur cycling at the Triassic-Jurassic boundary. *Geology* **37**, 835–838.

Wu N., Farquhar J., Strauss H., Kim S.-T. and Canfield D. E. (2010) Evaluating the S-isotope fractionation associated with Phanerozoic pyrite burial. *Geochim. Cosmochim. Acta* **74**, 2053–2071.

Yager J. A., West A. J., Corsetti F. A., Berelson W. M., Rollins N. E., Rosas S. and Bottjer D. J. (2017) Duration of and decoupling between carbon isotope excursions during the end-Triassic mass extinction and Central Atlantic Magmatic Province emplacement. *Earth Planet. Sci. Lett.* **473**, 227–236.

Zerkle A. L., Kamyshny, Jr, A., Kump L. R., Farquhar J., Oduro H. and Arthur M. A. (2010) Sulfur cycling in a stratified euxinic lake with moderately high sulfate: Constraints from quadruple S isotopes. *Geochim. Cosmochim. Acta* **74**, 4953–4970.

Ziegler P. A. (1988). Evolution of the Arctic-North Atlantic and the Western Tethys. American Association of Petroleum Geologists Memoir 43, 197 pp.

Zhang G., Zhang X., Li D., Farquhar J., Shen S., Chen X. and Shen Y. (2015) Widespread shoaling of sulfidic waters linked to the end-Guadalupian (Permian) mass extinction. *Geology* **43**, 1091–1094.

Zhang G., Zhang X., Hu D., Li D., Algeo T. J., Farquhar J., Henderson C. M., Qin L., Shen M., Shen D., Schoepfer S. D., Chen K. and Shen Y. (2017) Redox chemistry changes in the Panthalassic Ocean linked to the end-Permian mass extinction and delayed Early Triassic biotic recovery. *Proc. Natl. Acad. Sci.* **114**, 1806–1810.

Associate editor: Timothy Lyons